HHS Public Access

Author manuscript

Int J Fract. Author manuscript; available in PMC 2019 May 01.

Published in final edited form as:

Int J Fract. 2018 May ; 211(1-2): 203–216. doi:10.1007/s10704-018-0283-x.

An experimentally-calibrated damage mechanics model for stone fracture in shock wave lithotripsy

Daniel Fovargue,
Department of Mathematics, University of North Carolina, Chapel Hill, North Carolina, 27599-3250

Sorin Mitran,
Department of Mathematics, University of North Carolina, Chapel Hill, North Carolina, 27599-3250

Georgy Sankin,
Department of Mechanical Engineering and Materials Science, Duke University, Durham, North Carolina 27708

Ying Zhang, and
Department of Mechanical Engineering and Materials Science, Duke University, Durham, North Carolina 27708

Pei Zhong
Department of Mechanical Engineering and Materials Science, Duke University, Durham, North Carolina 27708

Abstract

A damage model suggested by the Tuler-Butcher concept of dynamic accumulation of microscopic defects is obtained from experimental data on microcrack formation in synthetic kidney stones. Experimental data on appearance of microcracks is extracted from micro-computed tomography images of BegoStone simulants obtained after subjecting the stone to successive pulses produced by an electromagnetic shock-wave lithotripter source. Image processing of the data is used to infer statistical distributions of crack length and width in representative transversal cross-sections of a cylindrical stone. A high-resolution finite volume computational model, capable of accurately modeling internal reflections due to local changes in material properties produced by material damage is used to simulate the accumulation of damage due to successive shocks. Comparison of statistical distributions of microcrack formation in computation and experiment allows calibration of the damage model. The model is subsequently used to compute fracture of a different aspect-ratio cylindrical stone predicting concurrent formation of two main fracture areas as observed experimentally.

1 Introduction

A fundamental understanding of the processes in shock wave lithotripsy (SWL) can suggest procedures to avoid undesired side effects such as kidney bleeding and edema [18]. Standard treatments require generation of a few thousand shocks to reduce a kidney stone to fragments of small enough size (~ 2mm) to be evacuated through the urinary tract. The basic

mechanism of stone fracture and comminution is considered to involve successive crack formation due to stresses induced in the stone by passing shock waves in conjunction with surface damage produced by collapsing cavitation bubbles [20, 9, 36]. The concept of dynamic fatigue arising from damage accumulation has been used [20, 37] to provide order of magnitude estimates of the number of shocks required to induce stone breakdown within the framework of the widely-used cohesive zone concept of brittle fracture [4]. Though several possible mechanisms have been proposed, detailed modeling of stone comminution presents challenges due to inherent material heterogeneity as well as dynamic changes in material properties as successive shocks lead to accumulation of cracks. Attempts have been made to account for material heterogeneity in an averaged sense using representative volume elements (RVE) [37]. As remarked in [37], length scales imposed by the incoming SWL pulse ($\sim 40\mu$m in the stone for a typical pulse rise time of 10 ns) can be smaller than the RVE characteristic length (ranging from 50μm for smooth cystine stones to 0.5mm for a struvite stone), thus limiting the validity of mean-field descriptions based upon RVEs. In fact, focalization phenomena within a stone may lead to even smaller length scales, a situation in which quantitatively correct prediction of fracture is possible only through fully numerical approaches.

Kidney stone comminution in SWL is a subset of the larger problem of fracture in brittle materials. Numerical simulation of the full comminution process is challenging due to the interaction of widely disparate scales: a continuum scale at which stress waves propagate through the material and a microscopic scale at which microcracks form (see, e.g., [27] for a review). Discrete crack models require complicated geometric tracking and formulation of a closure relation to provide crack tip velocities, typically through continuum-level momentum and energy conservation [25]. The geometric complexity of crack tracking can be alleviated in level-set methods [31], and a localized tip closure relation can be replaced by a diffuse zone such as in the cohesive zone concept [4] that recognizes that unresolved microcracks play a fundamental role in crack propagation in addition to conservation of momentum and energy. Unresolved processes at the continuum scale have recently been described through enriched basis methods (e.g., XFEM [1]) that supplement a finite element basis meant to capture continuum fields with stochastic representations of unresolved microcracks. Though these developments are promising, significant additional development would be needed to advance these methods from proof-of-concept problems to realistic applications in SWL. In particular, dynamic fracture behavior that arises from the accumulation of a large number of microcracks is difficult to model accurately with current deterministic fracture models (see [27] for a recent review).

Phenomenological models [30] eschew detailed computational modeling in favor of positing some statistical distribution of failure events (typically a Weibull distribution) in order to predict overall properties of the comminution process, such as the correlation of fragment sizes to SWL parameters under clinical control such as shock dosage and average peak pressure. Such relationships are important for practical lithotripter design, but lack detail on the comminution process and variability due to various stone types and geometric configurations.

Damage models [15] are at an intermediate level of description with respect to the above approaches. A continuum level description is used to resolve stress fields, but the material properties change in time due to the formation of microcracks. Damage models can be combined with partially resolved cracks [7]. As in all incompletely resolved models the key aspect is relating microcrack formation and growth to local stresses, and most current modeling relies on homogenized models such as the Griffith criterion [14] that compares the energy of the elastic strain to the surface energy of a new crack.

In this work we consider the issue of dynamic changes in material properties due to accumulation of damage. The tenet of this work is that first-principle models for crack initiation and propagation can be replaced by experimental calibration of posited damage models or extraction of a damage model through data assimilation procedures. The approach falls within the general class of stochastic fracture models [19, 26, 13], but adopts two main novel features: (1) calibration of damage model coefficients from experiments on a kidney stone simulant (BegoStone), and (2) use of adaptive mesh refinement to resolve microcrack aggregation into macrocracks that lead to stone fracture. Experimental databases of changes in crack configuration in a stone simulant due to successive impingement of shock waves are constructed from micro-tomography images. The data is used to extract statistical distributions of changes in the damaged microstructure. The statistical distributions serve as a stochastic closure model for numerical computations of elastic wave propagation in a heterogeneous medium representing the kidney stone. The elastic moduli are updated to take into account the accumulated damage, thus capturing internal reflections and transmission due to formation of internal fractures. Adaptive mesh refinement is used to keep track of crack formation processes. Model predictions on the location and shape of the first fracture of a cylindrical stone are compared to experimental results.

2 Methods

2.1 Elasticity equations and numerical solution

Stress ($\boldsymbol{\sigma}$) and displacement velocity ($\boldsymbol{u}$) in a stone are assumed to be accurately described by the linear elasticity equations [3, 28]. The conservation of momentum equations for a medium of mass density ρ

$$\rho \frac{\partial \boldsymbol{u}}{\partial t} = \nabla \cdot \boldsymbol{\sigma}, \quad (1)$$

are closed through the geometric relationship between strain ($\boldsymbol{\varepsilon}$) and displacements ($\boldsymbol{\delta}$,$\boldsymbol{u} = \dot{\boldsymbol{\delta}}$)

$$\boldsymbol{\varepsilon} = \frac{1}{2}(\nabla \boldsymbol{\delta} + (\nabla \boldsymbol{\delta})^T), \quad (2)$$

and the linear (Hooke) constitutive relation

$$\boldsymbol{\varepsilon} = \frac{1+\nu}{E}\boldsymbol{\sigma} - \frac{\nu}{E}\mathrm{Tr}(\boldsymbol{\sigma})\mathbf{I}, \quad (3)$$

with E the Young modulus, ν the Poisson ratio, $\mathrm{Tr}(\boldsymbol{\sigma})$ the trace of the stress, and $\mathbf{I}$ the identity matrix. The above equations can be reformulated as a system of partial differential equations [21]

$$\mathbf{q}_t + \mathbf{A}\mathbf{q}_x + \mathbf{B}\mathbf{q}_y + \mathbf{C}\mathbf{q}_z = \mathbf{0}, \quad (4)$$

for a vector containing the stress and velocity components

$$\mathbf{q} = \left(\sigma^{xx}\ \sigma^{yy}\ \sigma^{zz}\ \sigma^{xy}\ \sigma^{yz}\ \sigma^{xz}\ u\ v\ w\right)^T, \quad (5)$$

where $\mathbf{u} = (u\ v\ w)^T$, and matrices $\mathbf{A}$,$\mathbf{B}$,$\mathbf{C}$ are defined by the mass density ρ and Lamé parameters λ, μ. In particular,

$$\mathbf{A} = -\begin{pmatrix} 0 & 0 & 0 & 0 & 0 & 0 & \lambda+2\mu & 0 & 0 \\ 0 & 0 & 0 & 0 & 0 & 0 & \lambda & 0 & 0 \\ 0 & 0 & 0 & 0 & 0 & 0 & \lambda & 0 & 0 \\ 0 & 0 & 0 & 0 & 0 & 0 & 0 & \mu & 0 \\ 0 & 0 & 0 & 0 & 0 & 0 & 0 & 0 & 0 \\ 0 & 0 & 0 & 0 & 0 & 0 & 0 & 0 & \mu \\ 1/\rho & 0 & 0 & 0 & 0 & 0 & 0 & 0 & 0 \\ 0 & 0 & 0 & 1/\rho & 0 & 0 & 0 & 0 & 0 \\ 0 & 0 & 0 & 0 & 0 & 1/\rho & 0 & 0 & 0 \end{pmatrix}, \quad (6)$$

with $\mathbf{B}$,$\mathbf{C}$ of similar form obtained through permutation of components [21]. The matrices $\mathbf{A}$,$\mathbf{B}$,$\mathbf{C}$ admit a complete eigensystem, hence the system (4) is hyperbolic. Solving the eigenproblem $\mathbf{AR} = \mathbf{R\Lambda}$, gives eigenvalues

$$\mathrm{diag}(\mathbf{\Lambda}) = (-c_p, c_p, -c_s, c_s, -c_s, c_s, 0, 0, 0), \quad (7)$$

with $c_p = \sqrt{(\lambda+2\mu)/\rho}$ denoting the longitudinal or P-wave speed, and $c_s = \sqrt{\mu/\rho}$ denoting the transverse or S-wave speed. The eigenvectors of $\mathbf{A}$ are

$$\mathbf{R} = \begin{pmatrix} \lambda+2\mu & \lambda+2\mu & 0 & 0 & 0 & 0 & 0 & 0 & 0 \\ \lambda & \lambda & 0 & 0 & 0 & 0 & 0 & 1 & 0 \\ \lambda & \lambda & 0 & 0 & 0 & 0 & 0 & 0 & 1 \\ 0 & 0 & \mu & \mu & 0 & 0 & 0 & 0 & 0 \\ 0 & 0 & 0 & 0 & 0 & 0 & 1 & 0 & 0 \\ 0 & 0 & 0 & 0 & \mu & \mu & 0 & 0 & 0 \\ c_p & -c_p & 0 & 0 & 0 & 0 & 0 & 0 & 0 \\ 0 & 0 & c_s & -c_s & 0 & 0 & 0 & 0 & 0 \\ 0 & 0 & 0 & 0 & c_s & -c_s & 0 & 0 & 0 \end{pmatrix}, \quad (8)$$

with columns 1–2 giving forward and backward P-waves in the *x*-direction, columns 3–6 forward and backward shear waves in the *y*, *z*-directions. Remaining columns correspond to non-propagating modes. Again, the eigensystems for **B**,**C** can be obtained through permutation of components. The system (4) is discretized through a second-order accurate finite volume approach and advanced in time by dimensional splitting and a wave propagation algorithm [21] that decomposes jumps in **q** at finite volume cell interfaces into left- and right-propagating elastic waves. Of particular relevance to this study is the fact that the numerical method captures reflections and transmissions at interfaces of cells with different material properties, where the propagating eigenvectors are formulated as

$$\widetilde{\mathbf{R}} = \begin{pmatrix} (\lambda+2\mu)_L & (\lambda+2\mu)_R & 0 & 0 & 0 & 0 \\ \lambda_L & \lambda_R & 0 & 0 & 0 & 0 \\ \lambda_L & \lambda_R & 0 & 0 & 0 & 0 \\ 0 & 0 & \mu_L & \mu_R & 0 & 0 \\ 0 & 0 & 0 & 0 & 0 & 0 \\ 0 & 0 & 0 & 0 & \mu_L & \mu_R \\ (c_p)_L & -(c_p)_R & 0 & 0 & 0 & 0 \\ 0 & 0 & (c_s)_L & -(c_s)_R & 0 & 0 \\ 0 & 0 & 0 & 0 & (c_s)_L & -(c_s)_R \end{pmatrix}. \quad (9)$$

This allows accurate simulation of the modification of P-, S-wave propagation inside a stone due to accumulation of damage as reflected in changes in the values of the elastic moduli λ, μ. The amplitudes **a** of the wave components induced by a jump $\Delta\mathbf{q}$ at a cell interface are solutions of $\Delta\mathbf{q} = \widetilde{\mathbf{R}}\mathbf{a}$, with P-wave amplitudes

$$a_1 = \frac{(c_p)_R\delta_1 + M_R\delta_7}{b_R(c_P)_L + M_L(c_p)_R}, a_2 = \frac{(c_p)_L\delta_1 - M_L\delta_7}{b_R(c_P)_L + M_L(c_p)_R}, \quad (10)$$

with $M = \lambda + 2\mu$ denoting the P-wave modulus., and S-wave amplitudes

$$a_3 = \frac{(c_s)_R \delta_4 + \mu_R \delta_8}{(c_s)_R \mu_L + (c_s)_L \mu_R}, \quad a_4 = \frac{(c_s)_L \delta_4 - \mu_L \delta_8}{(c_s)_R \mu_L + (c_s)_L \mu_R}, \quad (11)$$
$$a_5 = \frac{(c_s)_R \delta_6 + \mu_R \delta_9}{(c_s)_R \mu_L + (c_s)_L \mu_R}, \quad a_6 = \frac{(c_s)_L \delta_6 - \mu_L \delta_9}{(c_s)_R \mu_L + (c_s)_L \mu_R}.$$

Transverse wave propagation corrections [21] ensure accurate capturing of transmitted and reflected components in regions where the material interface is not colinear with the computational grid. Fractured regions are assumed to have properties of the background medium, i.e., water.

2.2 Damage model

Damage models maintain the basic framework of linear elasticity, but modify the elastic moduli to take into account irreversible plastic deformation associated with appearance of unresolved microcracks. In the simplest formulation, the orientation of the unresolved microcracks is assumed to be uniformly distributed, leading to an isotropic damage law characterized by a single additional field variable D [17]. In a finite volume that has cross-section S, the presence of unresolved microcracks and cavities reduces the cross-sectional area by S_D, leading to the definition of the scalar damage

$$D = S_D / S. \quad (12)$$

As seen from Equation (12) the damage, D, ranges from 0 to 1, and 0 corresponds to a completely undamaged state. Some critical value, D_c, is specified which corresponds to the rupture of the element or the initiation of a macrocrack. This value typically ranges from 0.2 to 0.8 depending on the material. While damage models can be extended to account for anisotropic effects [22, 23, 33], the approach taken here is to assume that unresolved microcracks are isotropic and to fully resolve macrocracks in a kidney stone. Whereas in the absence of damage the local stress would be $\boldsymbol{\sigma}$, the presence of damage increases this to an effective local stress $\tilde{\boldsymbol{\sigma}} = \boldsymbol{\sigma}/(1 - D)$. This can readily be modeled by modifying the local values of the Lamé parameters to become $\tilde{\lambda} = \lambda(1 - D)$, $\tilde{\mu} = \mu(1 - D)$.

An additional equation modeling damage growth is needed to close the system of equations (4), which is given here in terms of the local principal stresses σ_1, σ_2, σ_3 and specific material properties. A damage law suitable for brittle materials [23, 16]

$$\frac{\mathrm{d}D}{\mathrm{d}t} = \alpha \sigma_c^s \left| \frac{\sigma_m}{\sigma_c} - 1 \right|^s, \quad (13)$$

is adopted, where σ_m is a maximum local stress, σ_c is a critical stress value denoting unresolved local failure (i.e., appearance of microcracks) and a, s are material properties describing crack nucleation and propagation. The damage law (13) conforms to the power-law model or Paris-law description of crack growth, a model with wide experimental support across a variety of materials [2]. Note that (13) corresponds to a cummulative Tuler-Butcher model [32] with (a, s) describing average damage production in time. The damage law (13) is applied only if $|\sigma_m| > |\sigma_c|$, otherwise no additional damage is produced $\mathrm{d}D/\mathrm{d}t = 0$. The material fails and a macrocrack appears if the maximum tensile stress $\sigma_T = \max(\sigma_1, \sigma_3)$ exceeds the material critical tensile strength $\sigma_{T,c}$, or if the minimum compressive stress $\sigma_C = -\min(\sigma_2, \sigma_3)$ is less than the critical compressive strength $\sigma_{C,c}$. In this work both processes are assumed to evolve damage at the same rate such that a single pair of parameters (a, s) is extracted from the data, though the thresholds $\sigma_{T,c}$ and $\sigma_{C,c}$ are allowed to have different values.

The material properties a, s, σ_c within the damage law (13) are determined by processes at an unresolved microscopic scale. Theoretical attempts at deriving analogous damage models (e.g., [20]) lead to wide variability in model predictions (i.e., by as much as two orders-of-magnitude difference in predictions of number of shocks to failure in [20]). This is a direct result of the complexity of the microscopic processes related to kidney stone failure that involves multiple possible mechanisms (e.g., spall, compression-induced tensile cracks). Rather than attempt a theoretical derivation of the damage law coefficients, the procedure put forward in this work is to use experimentally observed damage accumulation produced by passage of successive shocks as a statistical closure model.

2.3 Experimental set-up

Data for a statistical damage closure model is obtained from experiments on BegoStone artificial kidney stones with a powder-to-water mixing ratio of 5:1, with mechanical properties similar to calcium oxalate monohydrate and brushite stones. Cylindrical stones were placed in an electromagnetic (EM) shock wave generator with an acoustic lens to focalize pulses produced by the EM source at 14kV. The pulses propagate in 0.2 micrometer-filtered and degassed water (<3mg/l oxygen concentration at 23°C) within a Lucite tank of dimensions 40 × 30 × 30 cm (Fig. 1). Experimental pressure measurements obtained at various points near the lens focus compare favorably with the numerical simulations [12] of the focalization process that will furnish boundary conditions for the penetration of acoustic pulses into the stones (Fig. 2).

2.4 Micro-CT data

Micro-CT (μCT) images at a resolution of 6 μm (Scanco USA μCT 40 system, Wayne PA) were acquired of the initial state of the stones as well as after subjecting stones to shocks (Table 1). Stones were subjected to shocks until the first fracture of the stone was produced (Fig. 3).

Image data was processed to characterize the statistics of cracks produced in the stone by the passage of shocks. Cross-sections within the zone were processed individually. Strong absorption due to quasi-spherical voids in the stones were identified through a threshold and

eccentricity condition (Fig. 4a). Identified voids were filled in at the average image intensity level, and intensity levels were rescaled to cover entire range (0,1), thus highlighting the appearance of cracks against the variable background (Fig. 4b). Points within a crack were identified through a threshold (Fig. 4c), clustered and a skeleton representation was constructed for each cluster furnishing information on crack length and thickness. The implementation used for image processing is completely documented (Appendix of [11]).

2.5 Statistical model for experimentally-observed microcracks

The piecewise linear representation of microcracks resulting from μCT images is used to construct a statistical model of damage accumulation in a stone due to passage of successive shock waves. A parametric statistical distribution of microcrack length and thickness is sought. Analysis of the validity of the data conforming to a particular parametric distribution led to identification of the log-normal distribution

$$f(x;\mu,\sigma) = \frac{1}{x\sigma\sqrt{2\pi}} \exp\left[-\frac{(\ln x - \mu)^2}{2\sigma^2}\right],$$

at a significance level of $p = 0.05$, with all other common parametric distributions exhibiting $p > 0.1$. Figure 5 presents a comparison of the data and best-fit for the three closest statistical descriptions of the data.

Once the form of the parametric distribution has been established, μCT data obtained after each shock passage is used to construct log-normal distributions for resolved microcrack segment length and thickness (Fig. 6, Left). The evolution with shock number of the (μ,σ) of the log-normal distributions for microcrack segment lengths and widths in a transversal section at 2/3 of the stone length are represented in (Fig. 6, Right, top). The total crack volume in the stones is approximated as the product of length, width, and μCT slice thickness (6μm), and is represented in Fig. 6 (Right, bottom).

Several aspects of the measured data are worthy of further discussion.

1. Recall that the mean m and variance v for a log-normal distribution are given by $m = \exp(\mu + \sigma^2/2)$, $v = [\exp(\sigma^2) - 1]\exp(2\mu + \sigma^2)$. For the 7mm stone 1 data in (Fig. 6, Right, top), the increase in μ (width) from $\mu_6 = 3.6$ at shock number 6 to $\mu_{12} = 4.05$ at shock number 12 corresponds to an increase of the average width of micro-cracks observed through the μCT scan from $w_6 = 37\mu$m to $w_{12} = 57\mu$m, an increase of 54% in the average width, and well resolved by the μCT scan resolution of 6μm. Similar increases in crack width are observed for the other stones.

2. The micro-crack average length does not change with increasing shock number. For the 7mm stone, the average length is $\Delta a \cong 55\mu$m. Though surprising at first, the result is consistent with the scenario of crack propagation in these experiments. Measurements are made after each shock application, and growth of the average micro-crack length would only occur if crack growth occurs along the same direction. Experimental observations of the microcrack patterns (e.g.,

Fig. 4) indicate branching of the micro-cracks produced by each shock. Changes in local damage reorient the principal stresses in succeeding shocks, and it is expected that growth of the crack would occur along different directions in each shock. In short, crack growth does occur after each shock as new segments of approximately the same length and differing orientations. The length is constant since the applied shock intensity is constant. Width of the previously existing segments increases with each applied shock.

3. The overall fracture volume (Fig. 6, Right, bottom) does indeed grow with each shock, indicating accumulation of damage. The rates of growth, though comparable in magnitude, differ between the various stones, suggesting importance of the initial distribution of defects in the stone. The observed fracture volume growth rates were $\Delta V = 0.167, 0.433, 0.825$ mm^3/shock for 7 mm stone 1, stone, 10 mm stone, respectively. The difference in fracture volume growth rate between stones of the same size is smaller than that between stones of different sizes.

A consistency check can be made between the observed microcrack growth rate and the energy imparted to the material by each successive shock. The energy released per unit thickness ΔU by crack growth Δa is $\Delta U = (\sigma^2/2E)\pi(\Delta a)^2$. The number of new crack segments can be estimated as $n = \Delta V/(\Delta a \bar{w}^2)$. Using typical values for the 7 mm stones $\Delta V = 0.3$mm^3/shock, $\Delta a \cong \bar{w} \cong 50\mu$m, $n \cong 2400$ new crack segments are produced, and the corresponding tensile energy release is $\Delta U_{\text{tot}} = n\Delta UL = 0.3$ mJ, ($\sigma \cong 7$MPa, the onset of damage threshold cf. 3, $E = 9.2$GPa, $L = 7$mm). The energy density of a shock from the surrounding water medium is $W = p_{\max}^2/(\rho c^2)$, with $p_{\max} = 45$MPa (Fig. 2), and $\rho = 10^3$ kg/m^3, $c \cong 1500$m/s for water. The fraction of this shock energy that refracts into the stone is $f = (2\rho c)^2/(\rho c + \rho_s c_P)^2 \cong 0.22$, with stone density, P-wave speed from Table 2. If uniformly distributed, the energy within the newly created fracture volume would be $W_{\text{fr}} = fW\Delta V = 0.06$ mJ. Focalization of P, S-waves within the stone [35] lead to increases of stress by a factor of $c \cong 3$ (Fig. 8) leading to an estimate of the energy release in the fracture volume of $c^2 W_{\text{fr}} \cong 0.5$ mJ, of the same order of magnitude as $\Delta U_{\text{tot}} = 0.3$ mJ.

2.6 Damage model calibration

Microcracks observed in μCT images arise from a complex process of increased local stress due to focalization of P- and S-waves that propagate through the stone and interact with inherent material inhomogeneities and the additional internal interfaces associated with previous cracks. The objective of this study is to capture this process in a statistical sense through a prescribed damage evolution equation, e.g., the damage law (13). The critical tensile and compressive strengths $\sigma_{T,c}$, $\sigma_{C,c}$ are assumed to be known for the material of interest.

The main challenge in construction of computational fracture models is to balance modeling of homogenized effects of unresolved microcracks (damage) with the necessity of capturing a representative resolved crack pattern that leads to fracture. The approach adopted in this work is to determine the damage law (13) parameters (α, s) by comparison of probability

distributions of crack lengths and thickness obtained from experiment and numerical computation.

Let $D(n, t, \mathbf{x}; \alpha_k, s_k)$ denote the damage after n shocks at time t and position $\mathbf{x}$ within the stone as obtained by computation using the damage law (13) with model parameters α_k, s_k. Before application of any shocks the stone is assumed to have uniform damage $D(0, 0, \mathbf{x}; \alpha_k, s_k) = D_0$. Starting from a known damage configuration, $D(n, 0, \mathbf{x}; \alpha_k, s_k)$ the inhomogneous elasticity equations (4) are solved and the extremal tensile and compressive stresses within a stone are computed (Fig) starting from an initial grid with cell mesh size h. Additional damage is produced whenever $\sigma_T < \sigma_{T,c}$ or $\sigma_C < \sigma_{C,c}$. Adaptive mesh refinement [6, 5] is used to determine grid cells of size δ within the stone in which the damage exceeds a threshold indicating the formation of a microcrack $D > D_c$. After each shock passage the best-fit log-normal distributionbrittles of microcracks within transversal sections taken at 1/3, 1/2, 2/3, 3/4 of the stone axial dimension are determined leading to a parameter vector

$$\mathbf{p}^n(\alpha_k, s_k) = (\mu^n_{1/3}\ \sigma^n_{1/3}\ \mu^n_{1/2}\ \sigma^n_{1/2}\ \mu^n_{2/3}\ \sigma^n_{2/3}\ \mu^n_{3/4}\ \sigma^n_{3/4}). \quad (14)$$

The parameter vector $\mathbf{p}^n$ describing computational microcrack formation depends on the k^{th} approximation of the damage model parameters (α_k, s_k). The cummulative error between the computed microcrack statistical distribution $\mathbf{p}^n$ with respect to that extracted from experimental data $\mathbf{p}^n_{\text{exp}}$ is given by

$$F(\alpha_k, s_k) = \sum_{n=1}^{N_1} \|\mathbf{p}^n(\alpha_k, s_k) - \mathbf{p}^n_{\text{exp}}\|^2. \quad (15)$$

A gradient descent procedure is used to update the damage law parameters (α_k, s_k)

$$(\alpha_{k+1}, s_{k+1}) = (\alpha_k, s_k) - \lambda_k(\partial_\alpha F_k, \partial_s F_k), \quad (16)$$

until $\|(\partial_\alpha F_k, \partial_s F_k)\| < \varepsilon$, with $\partial_\alpha F_k = \partial F/\partial\alpha(\alpha_k, s_k)$, $\partial_s F_k = \partial F/\partial s(\alpha_k, s_k)$. The gradient of the error function F is approximated numerically, e.g., $\partial_\alpha F_k = [F(\alpha_k + d_\alpha, s_k) - F(\alpha_k - d_\alpha, s_k)]/(2d_\alpha)$.

Note that the above procedure propagates forward previous microcrack formation in the stone, capturing the discrete process of microcrack accumulation to formation of a fracture. Unresolved damage is also propagated forward by cell damage values $D < D_c$.

3 Results

To closely mimic experimental conditions, the actual geometry of a quasi-cylindrical stone of 7mm length and 5mm diameter was reconstructed from μCT data, including measured void geometry and slight misalignment of the stone with respect to the incoming pulse direction (Fig. 7). Material properties are given in Table 2. The stone is immersed in water and the voids within the stone are assumed to have same properties as water. Water is assumed to have a small S-wave speed to avoid singularity in the shear wave coefficients (11). Pulses with a peak pressure of $p_{\max} = 45$MPa are input as a $P-$ wave propagating into the computational domain from the left boundary along the x-direction. The computational domain of 12 × 10 × 10 mm is initially discretized with a 60 × 50 × 50 grid, with cell size $h = 200\mu$m. Adaptive mesh refinement (AMR) with three levels and refinement ratios (4, 4, 2) was used to obtain a minimal cell size $\delta = h/32 = 6.25\mu$m, close to the resolution of the μCT scan. An assumption of no initial damage was made $D(0, 0, \boldsymbol{x}) = 0$.

The inhomogeneous elasticity equations (4) are solved with a time step $\delta t = 69$ ns corresponding to a Courant number $\nu = c_{P,\max} \cdot \delta t/h = 0.98$, with time subcycling on finer grids within the AMR hierarchy. Typical density plots of the hydrostatic pressure $p = \text{trace}(\boldsymbol{\sigma})/3$ are presented in Fig. 8, in which the perturbative effect of the voids in the material are apparent.

The ultimate compressive and tensile strengths of the material were set as $\sigma_{C,\max} = -60$MPa, $\sigma_{T,\max} = 40$MPa, respectively. Any finest level cell in which the local stress values σ_C, σ_T exceeded these thresholds was flagged as a crack. The threshold for onset of damage was chosen as equal for both compression and tension $-\sigma_{C,c} = \sigma_{T,c} = 7.2$MPa. In any cell where local stress values exceeded these thresholds the damage law (13) was integrated forward in time. If the damage on a finest level cell exceeded $D_c = 0.5$, that cell was flagged as a microcrack. Initial values for the damage model parameters were chosen from Tuler and Butcher's orginal work to represent those for aluminum with $s_0 = 2$, $\alpha_0 = 5 \times 10^{-22}$ units of damage per Pa^{s0}, per second. The reasoning was to investigate qualitative difference in damage production in the BegoStone brittle material versus that of aluminum through any marked change in the exponent s, as well as to test the gradient descent procedure used in the minimization of the error function (15). Final values after 5 gradient descent iterations were $s = 1.4$ and $\alpha = 7.5 \times 10^{-18}$ units of damage per $\text{Pa}^{1.4}$ per second. These values are very close to the results $s = 1.3$, $\alpha = 8.9 \times 10^{-18}$ units of damage per $\text{Pa}^{1.3}$ per second obtained when using a parameter vector with only two independent components

$$\mathbf{p}^n(\alpha_k, s_k) = \left(\mu^n_{2/3} \;\; \sigma^n_{2/3}\right), \quad (17)$$

with the additional statistical parameters in the cross sections $i = 1/3, 1/2, 3/4$ taken as $(\mu^n_i, \sigma^n_i) = f_i \times (\mu^n_{2/3}, \sigma^n_{2/3})$. The fractions f_i are determined from the current maximal tensile stresses $\sigma_{T,i}$ in cross section i,

$$f_i = 1 - \frac{1}{2\mu_{2/3}} \log\left(\frac{\sigma_{T,i}}{\sigma_{T,2/3}}\right), \quad (18)$$

by comparison to those in the cross-section at 2/3 of the stone length. For the particular case of a cylindrical stone the focal region of maximal stress is well known to be at 2/3 of the stone length. For more complicated geometries, the full optimization procedure across statistical parameters in multiple cross sections might have to be used.

Typical evolution of damage and the appearance of microcracks in the material is shown in Fig. 9, computed with final (a, s) values, in which the position of the stone fracture compares favorably to that observed experimentally (Fig. 3).

The calibrated damage model was applied to an axisymmetric cylindrical stone of 10mm diameter and 1:1 aspect ratio to provide a more detailed numerical investigation of stress and damage patterns with results shown in Fig. 10. The axisymmetric computation was carried out on a fine grid with mesh size $h = 5\mu$m. Note the significant change in location of maximal tensile stress as damage accumulates in the stone, and the formation of two areas of fracture close to the distal surface and the middle transverse section of the stone. Experimental observations of such a stone (Fig. 11) also suggests formation of two observable fractures, one closer to the middle transverse section, but the other further from the distal boundary than obtained in the computational model. The computational model predicts full fracture after 10 shocks, as also observed experimentally (cf. Tabel 1).

4 Discussion

This work introduces a procedure to extract a calibrated damage model for kidney stone simulants and an adaptive mesh refinement approach to the representation of crack formation. The approach combines homogenized stochastic representation of damage production at length scales below the resolution threshold of the computational grid with tracking of resolved cracks through adaptive mesh refinement. The main benefit of the overall approach is that it offers an experimentally validated procedure that is computationally tractable, and can be extended to investigation of further fracturing and stone comminution. Though constructed for the specific case of shock-wave lithotripsy, the overall approach can readily be applied to other materials for which experimental data is available.

Within previous work on fracture of kidney stones, numerical computation of elastic wave propagation [8, 29] was considered in homogeneous stones in order to provide supporting data for various fracture mechanisms. As seen in the examples presented in this paper, both stone inhomogeneities and developing cracks have a significant effect upon fracture patterns. In particular in all cases considered here, a secondary fracture area appears ahead of the main fracture. The main fracture has been argued to occur at approximately 2/3 of the stone length based upon ray tracing arguments [35]. Within this interpretation the appearance of a secondary fracture area can be interpreted as arising from reflection of incoming shocks at

the interface formed by the first fracture. Elastic wave propagation in inhomogeneous media using methods closely related to the approach in this work, but without consideration of a damage model, have also been reported [10]. Work directly addressing fatigue in SWL [20, 37] has mostly concentrated on analytical estimates in order to provide estimates of the number of cycles needed for appearance of the first fracture, with results that can vary by orders of magnitude [20] in the predicted number of shocks, mainly attributed to the need for incorporation of experimental data to better characterize crack growth.

At this point, the overall model is incompletely tested since the damage model has been calibrated using data from only three stones and verified against experimental results of a single larger stone. The variability of the damage model parameters has to be investigated on a larger variety of stones in order to assess general applicability of the approach proposed here. As such, the main contribution from this paper is the overall framework for establishing an efficient model for computational fatigue based upon a combination of local grid refinement to follow larger cracks and a damage model for unresolved microcracks. It is useful to compare this approach to current work with XFEM methods (e.g., [24, 34]). The basic idea underlying XFEM is to enrich a finite element basis meant to resolve the mean field with additional degrees of freedom capable of capturing the effect of sharp interfaces. This same function is carried out by adaptive mesh refinement within the method proposed here.

Acknowledgments

This work was supported by NIH grant 5R37DK05298516. Authors thank anonymous reviewer for suggestions on manuscript improvement. DF carried out numerical implementation of elastic wave focusing in damaged media, image processing, statistical analysis and carried out experiments and μCT analysis. SM devised overall computational and experimental calibration approach, wrote computational package for AMR calculations, carried out damage model calibration and documented all procedures. GS, YZ aided in carrying out shock-wave experiments. PZ devised shock wave experiment, acoustic lens, Begostone preparation, and suggested importance of detailed study of stone fracture mechanisms.

References

1. Abdelaziz YazidHamouine Abdelmadjid. A survey of the extended finite element. COMPUTERS & STRUCTURES. Jun; 2008 86(11–12):1141–1151.
2. Anderson TL. Fracture Mechanics: Fundamentals and Applications. Taylor and Francis; Boca Raton, FL: 2005. 21
3. Asaro Robert J, Lubarda Vlado A. Mechanics of solids and materials. Cambridge University Press; 2006.
4. Barenblatt GI. The mathematical theory of equilibrium cracks in brittle fracture. Advances in Applied Mechanics. 1962; 7:55–129.
5. BERGER MJ, COLELLA P. Local adaptive mesh refinement for shock hydrodynamics. JOURNAL OF COMPUTATIONAL PHYSICS. May; 1989 82(1):64–84.
6. BERGER MJ, OLIGER J. Adaptive mesh refinement for hyperbolic partial-differential equations. JOURNAL OF COMPUTATIONAL PHYSICS. 1984; 53(3):484–512.
7. Camacho GT, Ortiz M. Computational modelling of impact damage in brittle materials. INTERNATIONAL JOURNAL OF SOLIDS AND STRUCTURES. Aug; 1996 33(20–22):2899–2938.
8. Cleveland RO, Sapozhnikov OA. Modeling elastic wave propagation in kidney stones with application to shock wave lithotripsy. JOURNAL OF THE ACOUSTICAL SOCIETY OF AMERICA. Oct; 2005 118(4):2667–2676. [PubMed: 16266186]

9. Coleman AJ, Saunders JE. A review of the physical properties and biological effects of the high amplitude acoustic field used in extracorporeal lithotripsy. Ultrasonics. 1993; 31:75–89. [PubMed: 8438532]
10. Fagnan KirstenLeVeque Randall J, Matula Thomas J. Computational models of material interfaces for the study of extracorporeal shock wave therapy. COMMUNICATIONS IN APPLIED MATHEMATICS AND COMPUTATIONAL SCIENCE. 2013; 8(1):159–194.
11. Fovargue D. PhD thesis. Department of Mathematics, University of North Carolina; Chapel Hill: 2014. Multiscale and multiphysics computational models of processes in shock wave lithotripsy.
12. Fovargue Daniel E, Mitran SorinSmith Nathan B, Sankin Georgy N, Simmons Walter N, Zhong Pei. Experimentally validated multiphysics computational model of focusing and shock wave formation in an electromagnetic lithotripter. JOURNAL OF THE ACOUSTICAL SOCIETY OF AMERICA. Aug; 2013 134(2, 2, SI):1598–1609. [PubMed: 23927200]
13. Grasa JorgeBea Jose AntonioDoblare Manuel. A probabilistic extended finite element approach: application to the prediction of bone crack propagation. In: Alfaiate J, Aliabadi MH, Guagliano M, Susmel L, editorsADVANCES IN FRACTURE AND DAMAGE MECHANICS VI, volume 348–349 of Key Engineering Materials; 6th International Conference on Fracture and Damage Mechanics; Madeira, PORTUGAL. JUL 17–19, 2007; 2007. 77
14. Griffith AA. The phenomenon of rupture and flow in solids. Phil Trans R Soc (London). 1921; 22:163–198.
15. Homand-Etienne F, Hoxha D, Shao JF. A continuum damage constitutive law for brittle rocks. COMPUTERS AND GEOTECHNICS. 1998; 22(2):135–151.
16. Kachanov LM. Introduction to Continuum Damage Mechanics. Martinus Nijhoff; Leiden: 1986.
17. LEMAITRE J. A continuous damage mechanics model for ductile fracture. JOURNAL OF ENGINEERING MATERIALS AND TECHNOLOGY-TRANSACTIONS OF THE ASME. 1985; 107(1):83–89.
18. Lingeman JE, Woods J, Toth PD, Evan AP, McAteer JA. The role of lithotripsy and its side effects. The Journal of urology. 1989; 141:793–797. [PubMed: 2645438]
19. Liu Wing KamQian DongGonella StefanoLi ShaofanChen WeiChirputkar Shardool. Multiscale methods for mechanical science of complex materials: bridging from quantum to stochastic multiresolution continuum. IN-TERNATIONAL JOURNAL FOR NUMERICAL METHODS IN ENGINEERING. Aug 20; 2010 83(8–9, SI):1039–1080.
20. Lokhandwalla M, Sturtevant B. Fracture mechanics model of stone comminution in eswl and implications for tissue damage. Physics in medicine and biology. 2000; 45:1923–1940. [PubMed: 10943929]
21. LeVeque RJ. Finite Volume Methods for Hyperbolic Problems. Cambridge Press; 2002.
22. Lemaitre JeanChaboche Jean-Louis. Mechanics of solid materials. Cambridge University Press; 1990.
23. Lemaitre JeanDesmorat Rodrigue. Engineering damage mechanics. Springer; New York: 2005. 23
24. Moes N, Dolbow J, Belytschko T. A finite element method for crack growth without remeshing. INTERNATIONAL JOURNAL FOR NUMERICAL METHODS IN ENGINEERING. Sep 10; 1999 46(1):131–150.
25. MORAN B, SHIH CF. Crack tip and associated domain integrals from momentum and energy-balance. ENGINEERING FRACTURE MECHANICS. 1987; 27(6):615–642.
26. Nouy A, Clement A, Schoefs F, Moes N. An extended stochastic finite element method for solving stochastic partial differential equations on random domains. COMPUTER METHODS IN APPLIED MECHANICS AND ENGINEERING. 2008; 197(51–52):4663–4682.
27. Rabczuk T. Computational methods for fracture in brittle and quasi-brittle solids: state-of-the-art review and future perspectives. ISRN Applied Mathematics. 2013; (849231):1–38.
28. Reddy JN. An introduction to continuum mechanics. Cambridge University Press; 2008.
29. Sapozhnikov Oleg A, Maxwell Adam D, MacConaghy BrianBailey Michael R. A mechanistic analysis of stone fracture in lithotripsy. JOURNAL OF THE ACOUSTICAL SOCIETY OF AMERICA. Feb; 2007 121(2):1190–1202. [PubMed: 17348540]

30. Smith Nathan B, Zhong Pei. A heuristic model of stone comminution in shock wave lithotripsy. JOURNAL OF THE ACOUSTICAL SOCIETY OF AMERICA. Aug; 2013 134(2, 2, SI):1548–1558. [PubMed: 23927195]

31. Stolarska M, Chopp DL, Moes N, Belytschko T. Modelling crack growth by level sets in the extended finite element method. INTERNATIONAL JOURNAL FOR NUMERICAL METHODS IN ENGINEERING. Jul 20; 2001 51(8):943–960.

32. TULER FR, BUTCHER BM. A criterion for the time-dependence of dynamic fracture. INTERNATIONAL JOURNAL OF FRACTURE. 1984; 26(4):322–328.

33. Voyiadjis George Z, Kattan Peter I. Damage mechanics. Taylor and Francis; Boca Raton, FL: 2005.

34. Wang YongxiangWaisman Haim. From diffuse damage to sharp cohesive cracks: a coupled xfem framework for failure analysis of quasi-brittle materials. COMPUTER METHODS IN APPLIED MECHANICS AND ENGINEERING. Feb 1.2016 299:57–89.

35. Zhang YingNault IsaacMitran SorinIversen Edwin S, Zhong Pei. Effects of stone size on the comminution process and efficiency in shock wave lithotripsy. ULTRASOUND IN MEDICINE AND BIOLOGY. Nov; 2016 42(11):2662–2675. [PubMed: 27515177]

36. Zhu SL, Cocks FH, Preminger GM, Zhong P. The role of stress waves and cavitation in stone comminution in shock wave lithotripsy. ULTRASOUND IN MEDICINE AND BIOLOGY. May; 2002 28(5):661–671. [PubMed: 12079703]

37. Zohdi TI, Szeri Andrew J. Fatigue of kidney stones with heterogeneous microstructure subjected to shock-wave lithotripsy. Journal of Biomedical Materials Research - Part B Applied Biomaterials. 2005; 75:351–358.

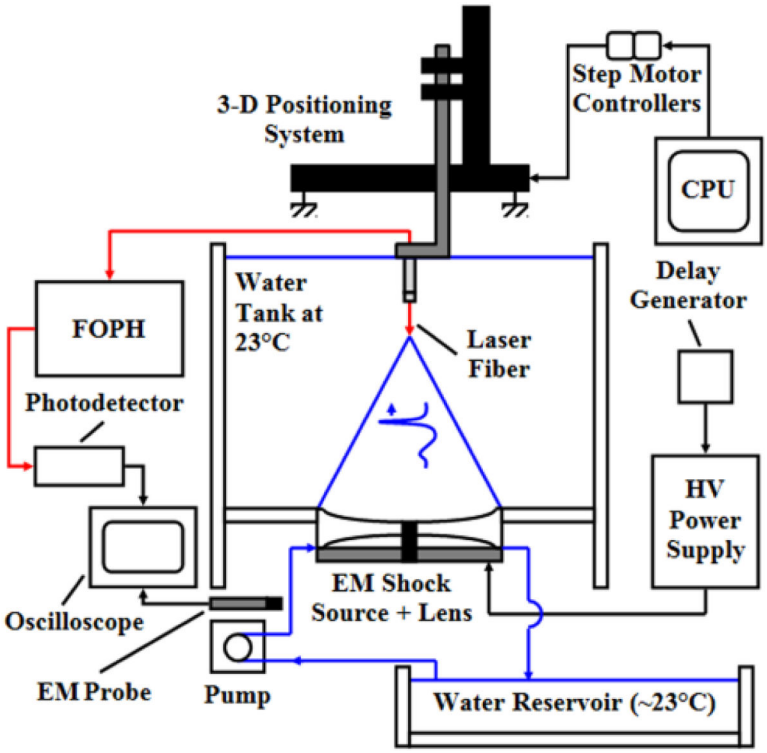

Figure 1.
Schematic of experimental setup.

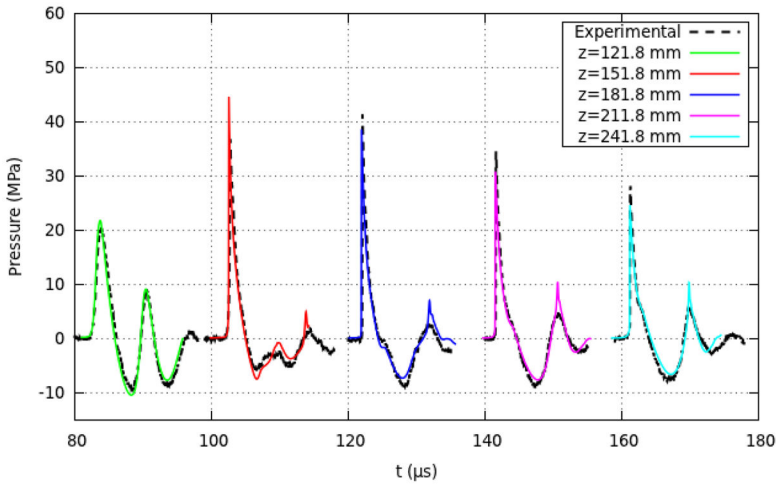

Figure 2.
Comparison of numerical and experimental pressure pulses [12]

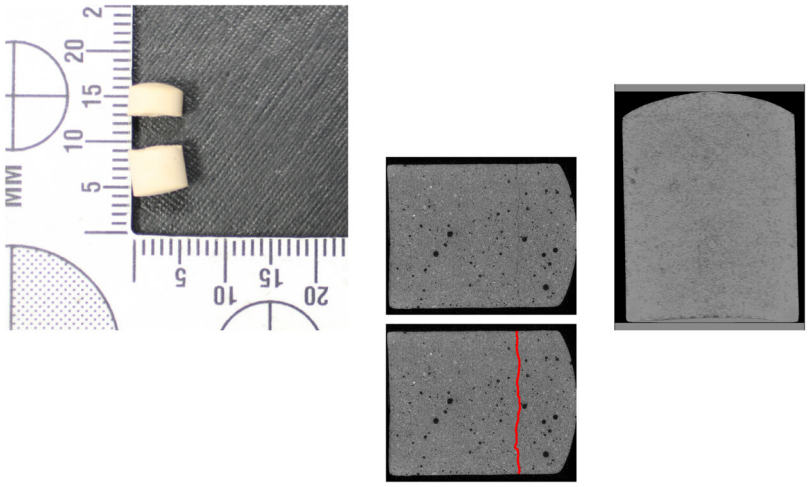

Figure 3.

Left: Cylindrical BegoStone sample after first fracture. Middle: μCT transversal image at production of first fracture with identification of fracture shape. Right: Transversal image of stone before application of shocks with voids filled in at average background to highlight any pre-existing cracks. Small cracks are observed, but away from the area of first fracture.

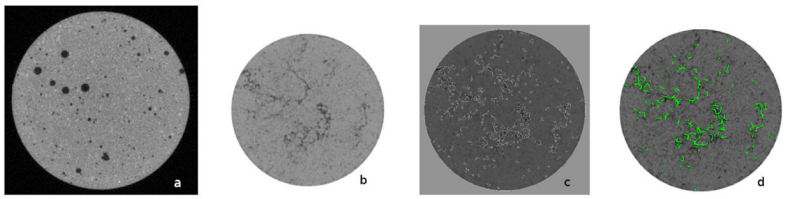

Figure 4.

Succession of image processing steps: (a) initial μCT image; (b) image after void elimination; (c) crack identification; (d) crack skeletons.

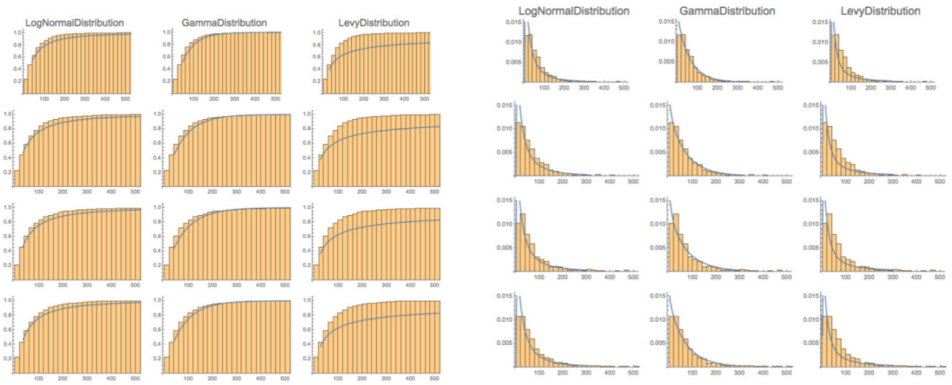

Figure 5.

Comparison of data and best-fit parametric distributions for three closest descriptions of microcrack segment length (in μm) obtained from μCT images of a 7mm cylindrical stone subjected to 12 shocks. Rows show data and best fits at 1/3, 1/2, 2/3 and 3/4 of the stone length. Left: cummulative probability density. Right: probability density.

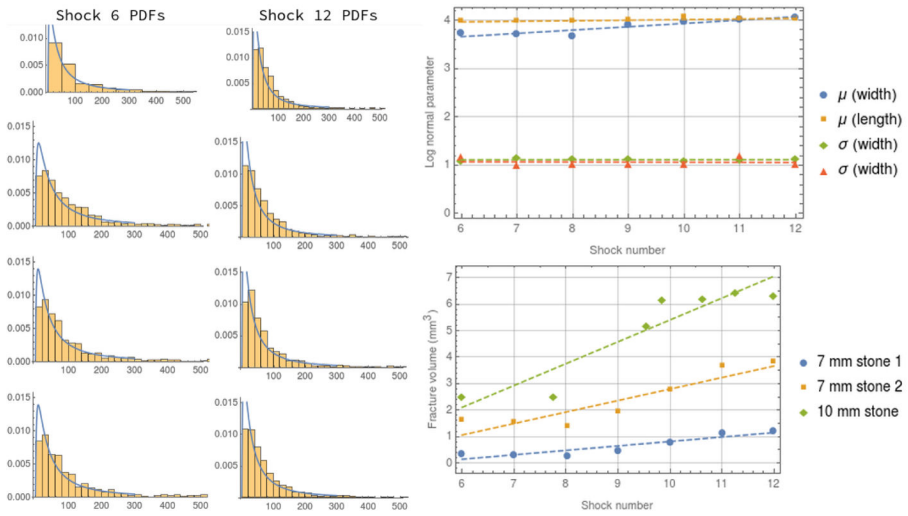

Figure 6.

Evolution of micro-crack statistics with increasing number of shocks. (Left) Microcrack length (μm) histograms and log-normal PDF best fits at 1/3, 1/2, 2/3 and 3/4 of the 7mm stone 1. (Right, top) Evolution of log-normal PDF parameters with shock number. (Right, bottom) Evolution of fracture volume with shock number.

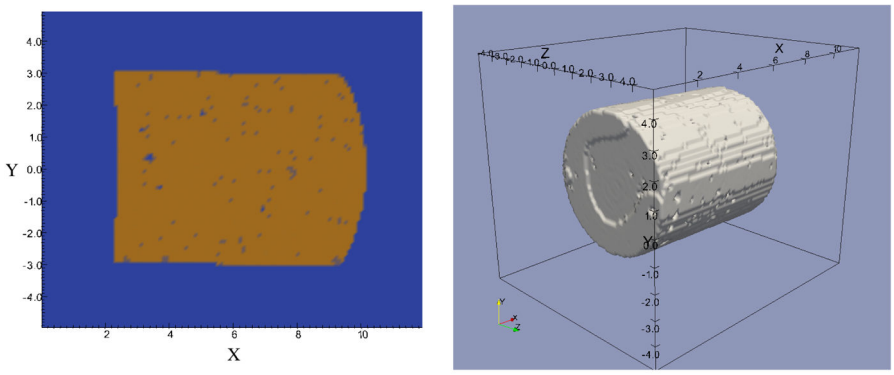

Figure 7.

Computational model setup. Left: Longitudinal cross-section through the stone showing measured void geometry and alignment with incoming pulse that propagates from left boundary along *x*-direction. Right: Three-dimensional perspective of actual stone geometry.

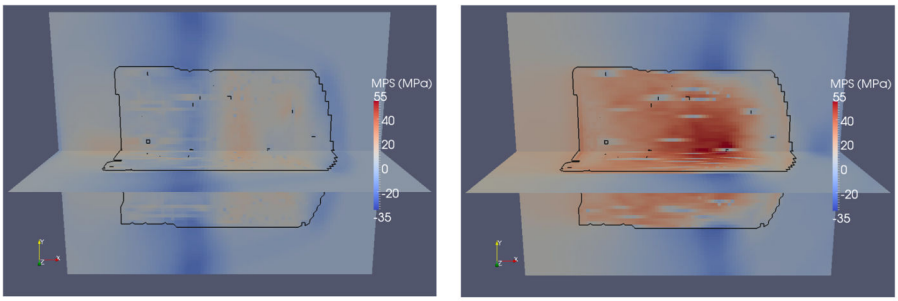

Figure 8.

Contours of the stress tensor trace (pressure). Left: At $t = 1.86$ ns after pulse impingement onto proximal surface of stone. Right: After reflection on distal surface and resultant focalization ($t = 3.71$ ns).

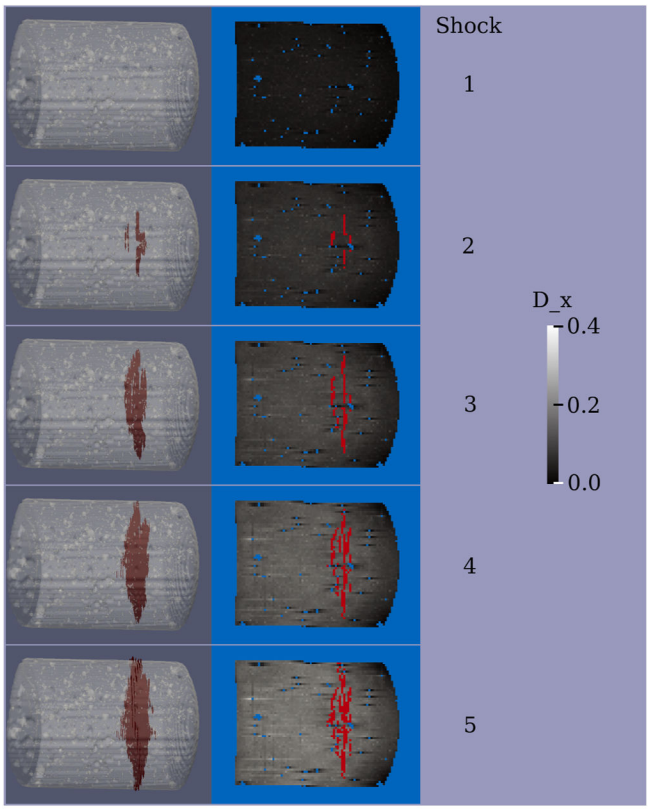

Figure 9.
Evolution of fractured cells after passage of successive shocks. Left: three-dimensional representation of cracks (red) and voids (white). Right: Longitudinal cross-section showing cracks and damage evolution.

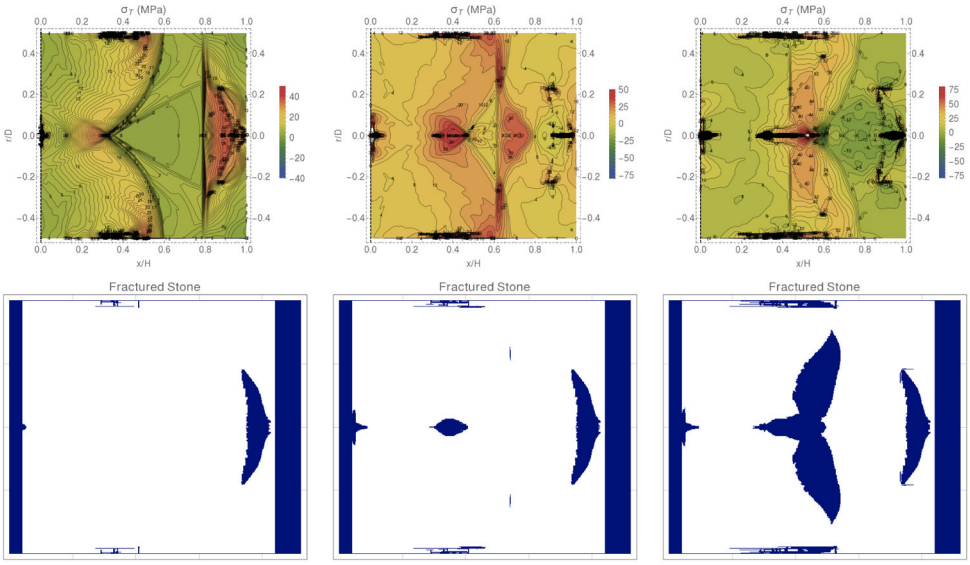

Figure 10.

Detailed evolution of formation of fracture in a cylindrical stone of 1:1 aspect ratio. Top row: Maximum tensile stress throughout the stone after 3,6,9 shocks. Bottom row: Cells with damage $D > 0.5$.

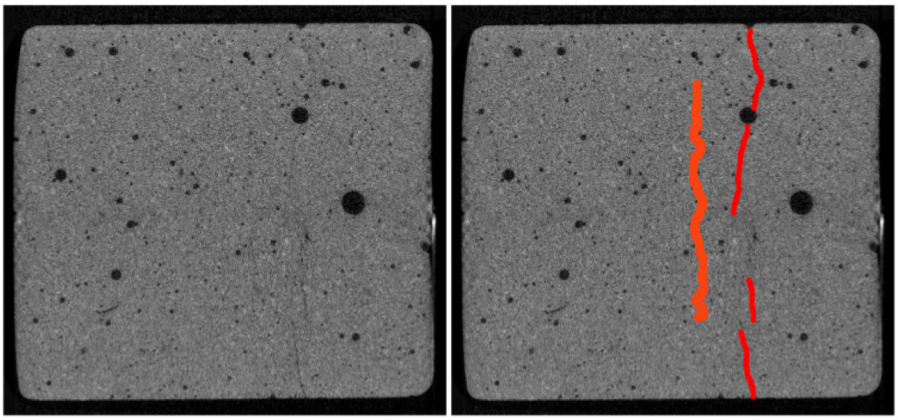

Figure 11.
Experimentally observed fracture in 10mm 1:1 aspect ratio cylindrical stone.

Table 1

Schedule of μCT image acquisition, with indication of images with resolved cracks within the stone (bold values)

Stone diameter/length (mm)	Number of Shocks
5/7	0 2 3 4 5 6 7 8 **9** **10** **11** **12**
5/7	0 3 4 **5** **6** **7** **9** **11** **13** **15**
9/10	0 5 **10** **15** **16** **18** **20** **22** **24**

Author Manuscript

Author Manuscript

Author Manuscript

Table 2

Material properties

Material	**Density ρ (kg/m^3)**	**c_P (m/s)**	**c_S (m/s)**
5:1 Begostone	1700	2840	1430
water	1000	1482	1